Chiral Dynamics of Few- and Many-Nucleon Systems

Evgeny Epelbaum[1] and Ulf-G. Meißner[2,3]

[1]Institut für Theoretische Physik II, Ruhr-Universität Bochum, D-44780 Bochum, Germany; email: evgeny.epelbaum@rub.de

[2]Helmholtz-Institut für Strahlen- und Kernphysik and Bethe Center for Theoretical Physics, Universität Bonn, D-53115 Bonn, Germany; email: meissner@hiskp.uni-bonn.de

[3]Forschungszentrum Jülich, Institut für Kernphysik, Institute for Advanced Simulation, and Jülich Center for Hadron Physics, D-52425 Jülich, Germany

Annu. Rev. Nucl. Part. Sci. 2012. 62:159–85

The *Annual Review of Nuclear and Particle Science* is online at nucl.annualreviews.org

This article's doi:
10.1146/annurev-nucl-102010-130056

0163-8998/12/1123-0159$20.00

Keywords

QCD, chiral symmetry, effective field theory, nuclear forces, lattice simulations, nuclear physics

Abstract

This review briefly introduces the chiral effective field theory of nuclear forces and atomic nuclei. We discuss the status of the nuclear Hamiltonian derived in this framework and some recent applications in few-nucleon systems. We also introduce nuclear lattice simulations as a new tool to address the many-body problem and present some of the first results based on that method.

Contents

1. INTRODUCTION AND DISCLAIMER

Nuclear physics on one hand is an old and well-established science but on the other hand represents a new and fascinating field. This is related to new experimental facilities and techniques and, even more so, to recent developments in theory. Using modern high-performance computers, physicists have made the first attempts to calculate atomic nuclei directly from quantum chromodynamics (QCD), the $SU(3)_{\text{color}}$ gauge theory of quarks and gluons (1). Complementary to these efforts, starting from the groundbreaking work by Weinberg (2), an effective field theory (EFT) approach to the forces between two, three, and four nucleons has been developed and applied to various nuclear-bound states and reactions. This EFT is based on the observations that (*a*) nuclei are composed of nonrelativistic nucleons (neutrons and protons) and virtual mesons and (*b*) the nuclear interactions feature two very distinct contributions, long-range one- and two-pion exchanges and shorter-range interactions, that can be represented by a tower of multinucleon operators. Given that the pion is the pseudo-Goldstone boson of the approximate chiral symmetry of QCD (for an introduction, see, e.g., Reference 3), its interactions with the nucleons are of derivative nature and are strongly constrained by the available data on pion-nucleon (πN) scattering and other fundamental processes. However, in harmony with the principles underlying EFT (for an introduction, see, e.g., Reference 4), one must also consider operators of nucleon fields only. In a meson exchange model of the nuclear forces, these can be represented by the exchanges of heavier mesons such as σ, ρ, ω, and so on—but such modeling is no longer necessary and does not automatically generate all the structures consistent with the underlying symmetries. Also, in the EFT approach, the forces between three and four nucleons are generated consistently with the dominant two-nucleon forces (2NFs)—which could never have been achieved in earlier models of these forces.

Due to the nonrelativistic nature of nuclei, the underlying equation for the nuclear A-body system (where A is the atomic number) to be solved is the Schrödinger equation, in which the various contributions to the nuclear potential are organized according to the power counting discussed below. In a second step, bound and scattering states are calculated as solutions of this equation. This process allows one not only to pin down the various low-energy constants (LECs) related to the multinucleon interactions but also to check the convergence of the approach by including higher orders in the underlying potentials. Once data for the two- and three-nucleon systems are described with sufficient precision, one can then perform ab initio calculations of

nuclei, eventually combining well-developed many-body techniques with the forces from chiral nuclear EFT. Another way to approach light and medium-heavy nuclei is based on simulation techniques because they are so successfully utilized in lattice QCD (5) to calculate the properties of protons, neutrons, and many other hadrons. All these developments are accompanied and extended by the construction of the corresponding electroweak charge and current operators that allow for many further fine tests of the structure of nuclei, as well as the calculation of fundamental nuclear reactions that are relevant to the generation of the elements in the big bang and in stars.

Disclaimer: Clearly, this is not a detailed, all-purpose review of this field; rather, we intend to provide an introduction to the underlying ideas and some recent applications. Two recent, detailed review articles can be found in References 6 and 7, which also contain many references to earlier work. We therefore have not attempted to give a complete or exhaustive list of references, but the interested reader will find sufficient citations to the literature to be able to acquire a much deeper understanding.

Our article is organized as follows. Section 2 contains the basic ideas of the chiral Lagrangian and power counting of the nuclear forces. We end that section with a brief review of the current status of the nuclear Hamiltonian derived in this framework. Section 3 contains some applications of these forces to nuclei that are based on calculations using exact few-nucleon methods. In Section 4, we present the new method of nuclear lattice simulations (nuclear lattice EFT) and discuss some of the first results obtained in that scheme.

2. FROM THE EFFECTIVE CHIRAL LAGRANGIAN TO NUCLEAR FORCES

Our goal is to develop a systematic and model-independent theoretical framework that can describe reactions involving several nucleons up to a center-of-mass (CMS) three-momenta of (at least) the order of the pion mass M_π. Following the usual philosophy of EFT, we aim at the most general parameterization of the amplitude consistent with fundamental principles such as Lorentz invariance, cluster separability, and analyticity. Given that the energies of the nucleons we are interested in are well below the nucleon mass, it is natural and appropriate to make use of the nonrelativistic expansion (i.e., an expansion in inverse powers of the nucleon mass, m_N). Accordingly, in the absence of external probes and below the pion production threshold, we are left with a potential theory in the framework of the quantum-mechanical A-body Schrödinger equation,

$$(H_0 + V)|\Psi\rangle = E|\Psi\rangle, \text{ where } H_0 = \sum_{i=1}^{A} \frac{-\vec{\nabla}_i^2}{2m_N} + \mathcal{O}(m_N^{-3}). \qquad 1.$$

The main task then reduces to the determination of the nuclear Hamilton operator $H_0 + V$. This task can be accomplished by use of the framework of chiral perturbation theory (ChPT) (2). Note that the approach outlined above automatically maintains unitarity of the scattering amplitude and correctly reproduces its analytic properties at very low energies. Consider, for example, the singularities of the neutron-proton (np) lth partial-wave amplitude in the complex energy plane with $E = k^2/m_N$ (**Figure 1**). The discontinuity across the right-hand cut running from $E = 0$ to $E = +\infty$ and separating the physical and unphysical sheets is determined by elastic unitarity, which is already built into the Lippmann–Schwinger (LS) equation. However, the left-hand cuts are governed by the properties of the interactions. Exploiting only the knowledge of the finite-range nature of the nuclear force and parameterizing the nucleon-nucleon (NN) potential by zero-range terms are sufficient to correctly describe the analytic structure of the amplitude within the region near threshold, limited by the branch point of the first left-hand cut associated

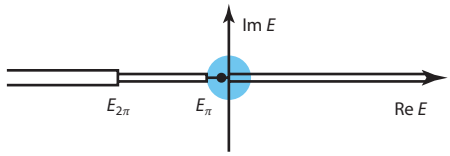

Figure 1

Singularity structure of the partial-wave two-nucleon scattering amplitude in the complex energy plane. The solid dot indicates the position of the *S*-wave (virtual) bound state. The shaded area shows the region in which the effective range function $k^{2l+1}\cot\delta_l(k)$ is a meromorphic function of k^2.

with one-pion exchange and located at $k^2 = -M_\pi^2/4$. The so-called pionless EFT (see Reference 8 for a recent overview) is based on the Lagrangian involving all possible zero-range two- and more-nucleon operators with increasing number of derivatives and can, in the two-nucleon sector, be matched to the well-known effective-range expansion, namely the expansion of the function $k^{2l+1}\cot\delta_l(k)$ in powers of k^2. Clearly, this approach is limited to very low energies that correspond to nucleon momenta well below the pion mass (**Figure 1**). To extend the range of applicability, one needs to correctly describe the left-hand singularities of the amplitude and thus to explicitly include in the potential the contributions emerging from the exchange of one or several pions. In the following subsections, we describe how this task can be accomplished in a systematic way by exploiting the spontaneously broken, approximate chiral symmetry of QCD. Another method to construct the *NN* scattering amplitude is dispersion theory; see Reference 9 for a recent application of this approach.

2.1. Chiral Lagrangian and Power Counting

Within the framework of ChPT, one derives nuclear forces from the most general effective chiral Lagrangian by making an expansion in powers of the small parameter q, defined as[1]

$$q \in \left\{ \frac{M_\pi}{\Lambda}, \frac{|\vec{k}|}{\Lambda} \right\}, \qquad 2.$$

where $Q \sim |\vec{k}| \sim M_\pi$ is a typical external momentum (the soft scale) and Λ is a hard scale. Appropriate powers of the inverse of this scale determine the size of the renormalized LECs in the effective Lagrangian. Note that once renormalization of loop contributions is carried out and the renormalization scale is set to $\mu \sim M_\pi$, as appropriate in ChPT, all the momenta flowing through the diagrams appear to be, effectively, of the order $\sim M_\pi$ (10). Consequently, one can use naïve dimensional analysis to estimate the importance of the (renormalized) contributions of individual diagrams.

Specifically, consider a connected Feynman graph with N nucleon lines.[2] It is easier to count the powers of the hard scale Λ rather than of the soft scale Q by observing that the only way for Λ to emerge is through the corresponding LECs. Thus, the low-momentum dimension ν of a given diagram can be expressed in terms of the canonical field dimensions, $\kappa_i + 4$, of V_i vertices of type i via

$$\nu = -2 + \sum V_i \kappa_i, \quad \text{where } \kappa_i = d_i + \frac{3}{2} n_i + p_i - 4. \qquad 3.$$

[1] Below, we use this parameter and the soft scale Q synonymously.

[2] Nucleons cannot be destroyed or created within the nonrelativistic approach.

Here, n_i (p_i) and d_i refer to the number of the nucleon (pion) field operators and derivatives or pion mass insertions, respectively. The constant -2 in the expression for ν is merely a convention. The power counting can also be rewritten in terms of topological variables, such as the number of loops L and nucleon lines N rather than κ_i, which is appropriate for diagrammatic approaches. For connected diagrams, the above equation takes the form

$$\nu = -4 + 2N + 2L + \sum V_i \Delta_i, \quad \text{where } \Delta_i = d_i + \frac{1}{2} n_i - 2. \tag{4.}$$

The chiral symmetry of QCD guarantees that Goldstone bosons, which in the case of two light flavors are identified with the pions, couple only through vertices involving derivatives or powers of M_π. This observation implies that the effective Lagrangian contains only irrelevant (i.e., non-renormalizable) interactions with $\kappa_i \geq 1$ ($\Delta_i \geq 0$), which allows for a perturbative description of pion-pion ($\pi\pi$) and πN scattering as well as nuclear forces. The leading interactions, namely the ones with the smallest possible Δ_i (that is, $\Delta_i = 0$), have the form

$$\begin{aligned} L^{(0)} = {} & \frac{1}{2}\partial_\mu \boldsymbol{\pi}\, \partial^\mu \boldsymbol{\pi} - \frac{1}{2} M_\pi^2 \boldsymbol{\pi}^2 + N^\dagger \left[i\partial_0 + \frac{g_A}{2F_\pi} \boldsymbol{\tau} \vec{\sigma} \vec{\nabla} \boldsymbol{\pi} - \frac{1}{4F_\pi^2} \boldsymbol{\tau} (\boldsymbol{\pi} \times \dot{\boldsymbol{\pi}}) \right] N \\ & - \frac{1}{2} C_S (N^\dagger N)(N^\dagger N) - \frac{1}{2} C_T (N^\dagger \vec{\sigma} N)(N^\dagger \vec{\sigma} N) + \cdots, \end{aligned} \tag{5.}$$

where $\boldsymbol{\pi}$ and N refer to the pion and nucleon field operators, respectively, and $\vec{\sigma}(\boldsymbol{\tau})$ denote the spin (isospin) Pauli matrices. Further, $g_A(F_\pi)$ is the nucleon axial coupling (pion decay) constant, and $C_{S,T}$ are the LECs accompanying the leading contact operators. The ellipses refer to terms involving additional pion fields. Importantly, chiral symmetry leads to highly nontrivial relations between the various coupling constants. For example, the strengths of all $\Delta_i = 0$ vertices without nucleons with 2, 4, 6,... pion field operators are given in terms of F_π and M_π. Similarly, all single-nucleon $\Delta_i = 0$ vertices with 1, 2, 3,... pion fields are expressed in terms of only two LECs, namely g_A and F_π. See References 11 and 12 for further details on the construction of the effective chiral Lagrangians (for a modern way to construct the pertinent πN Lagrangian, see, e.g., Reference 13).

The expressions for the power counting given above are derived under the assumption that there are no infrared divergences. This assumption is violated for a certain class of diagrams involving two and more nucleons due to the appearance of pinch singularities of the following kind:

$$\int dl_0 \frac{i}{l_0 + i\epsilon} \frac{i}{l_0 - i\epsilon}. \tag{6.}$$

Here, $i/(l_0 + i\epsilon)$ is the free nucleon propagator in the heavy-baryon approach corresponding to the Lagrangian in Equation 5. Clearly, the divergence is not "real" but merely an artifact of the extreme nonrelativistic approximation for the propagator, which is not applicable in that case. If we keep the first correction beyond the static limit, the nucleon propagator takes the form $i/(l_0 - \vec{l}^2/(2m_N) + i\epsilon)^{-1}$, leading to a finite result for the integral in Equation 6 that is, however, enhanced by a factor $m_N/|\vec{q}|$ compared with the estimation based on naïve dimensional analysis. In physical terms, the origin of this enhancement is related to the two-nucleon Green's function of the Schrödinger equation (Equation 1). The nuclear potential V we are actually interested in is, of course, well defined in the static limit $m_N \to \infty$ and thus is not affected by the above-mentioned infrared enhancement. The precise relation between the nuclear potentials and the amplitude corresponding to a given Feynman diagram is discussed in the next section.

We now address the qualitative implications of the power counting in Equation 4 and the explicit form of the effective chiral Lagrangian. First, one observes that the dominant contribution to the nuclear force arises from two-nucleon tree-level diagrams with the lowest-order vertices,

which implies that the nuclear force is dominated by the one-pion exchange potential and the two contact interactions without derivatives. Pion loops are suppressed by two powers of the soft scale. Also, vertices with $\Delta_i > 0$ that involve additional derivatives are suppressed and do not contribute at lowest order. Second, one observes the suppression of many-body forces: According to Equation 4, N-nucleon forces begin to contribute at order Q^{-4+2N}. This observation implies the dominance of the 2NF with three- and four-nucleon forces (3NFs and 4NFs) that appear as corrections at orders Q^2 and Q^4, respectively.

2.2. Derivation of the Nuclear Forces

We now clarify the meaning of the nuclear potential V and outline some approaches that can be used to derive it. We first rewrite Equation 1 as the LS equation for the half-shell T-matrix,

$$T_{\alpha\beta} = V_{\alpha\beta} + \sum_\gamma V_{\alpha\gamma} \frac{1}{E_\beta - E_\gamma + i\epsilon} T_{\gamma\beta}, \qquad 7.$$

where α, β, and γ denote the few-nucleon states; E_α is the kinetic energy of the nucleons in the state α; and $\sum_\gamma$ is interpreted as a sum (integral) over all discrete (continuous) quantum numbers of the nucleons. Further, the scattering matrix S, which is related to the T-matrix via

$$S_{\alpha\beta} = \delta(\alpha - \beta) - 2\pi i \delta(E_\alpha - E_\beta) T_{\alpha\beta}, \qquad 8.$$

can be directly computed from the effective chiral Lagrangian through the use of the Feynman graph technique. Doing so then allows one to define the potential $V_{\alpha\beta}$ by matching the amplitude to the iterative solution of Equation 7, which in the operator form can be written as

$$\hat{T} = \hat{V} + \hat{V}\,\hat{G}_0\,\hat{V} + \hat{V}\,\hat{G}_0\,\hat{V}\,\hat{G}_0\,\hat{V} + \cdots, \qquad 9.$$

where $\hat{G}_0$ is the A-nucleon resolvent operator. The outlined approach is, of course, not new and was extensively used in the 1950s in the context of the meson field theory (see, e.g., References 14 and 15). There is, however, a subtlety here related to the fact that the T-matrix calculated from the effective Lagrangian by utilizing Feynman diagrams and by the use of Equation 8 is available only on the energy shell. The potential to be substituted in the LS equation is needed off the energy shell, which leads to an ambiguity in the definition of the potential corresponding to the freedom associated with carrying out an off-the-energy-shell extension. This finding should not come as a surprise, given that the Hamiltonian $H_0 + V$ is not an observable quantity.

An alternative method to define nuclear forces exploits another old idea of decoupling the pion states from the rest of the Fock space by means of a suitably chosen unitary transformation (16). This approach was formulated in the context of chiral EFT in Reference 17. The derivation of the unitary operator, nuclear forces, and currents can be carried out straightforwardly by using perturbation theory in powers of Q and by employing the "algebraic" version of the power counting in Equation 3. The above-mentioned ambiguity of the nuclear potentials and currents can be systematically explored in this approach by performing further unitary transformations after decoupling the pion states. Interestingly, this ambiguity is strongly constrained by the renormalizability of the Hamiltonian (18).

Specifically, consider the derivation of the long-range two-nucleon potentials up to next-to-next-to-leading order ($\mathrm{N^2LO}$). For the sake of simplicity, here we use the matching approach and closely follow Reference 19 (also see Reference 20 for a pioneering calculation within the framework of time-ordered perturbation theory). We do not consider the short-range part of the nuclear force because it can be directly read off from the Lagrangian. Note that it is not necessary to explicitly evaluate pion loop diagrams involving contact interactions unless one is interested in

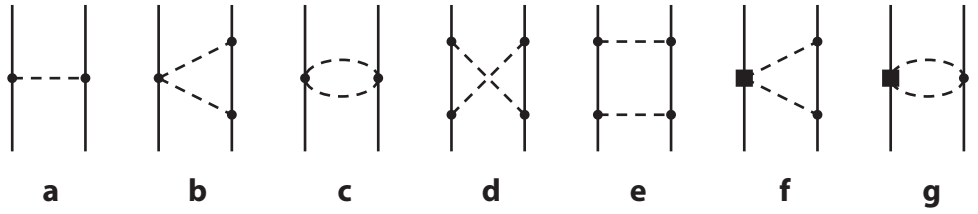

Figure 2

Diagrams contributing to the long-range part of the two-nucleon potential at (*a*) leading order, (*b–e*) next-to-leading order, and (*f*,*g*) next-to-next-to-leading order. The solid and dashed lines represent nucleons and pions, respectively. The solid dots and filled rectangles, respectively, refer to the leading ($\Delta_i = 0$) and subleading ($\Delta_i = 1$) vertices from the chiral Lagrangian.

the quark mass dependence of the short-range operators. As noted above, the leading-order (LO) contribution $\sim Q^0$ is due to one-pion exchange. Evaluating the contribution from the diagram in **Figure 2*a*** for on-shell nucleons yields

$$V_{1\pi}^{(0)} = T_{1\pi}^{(0)}|_{E_{\vec{p}}=E_{\vec{p}'}} = -\left(\frac{g_A}{2F_\pi}\right)^2 \frac{\vec{\sigma}_1\cdot\vec{q}\;\vec{\sigma}_2\cdot\vec{q}}{\vec{q}^{\,2}+M_\pi^2}\boldsymbol{\tau}_1\cdot\boldsymbol{\tau}_2, \qquad 10.$$

where $\vec{q} = \vec{p}\,' - \vec{p}$ is the nucleon momentum transfer; $\vec{p}$ and $\vec{p}\,'$ refer to the CMS initial and final momenta. Note that although $V_{1\pi}^{(0)}$ is uniquely defined in this procedure in the static limit with $E_{\vec{p}} = E_{\vec{p}'} = 0$, the relativistic corrections are not because one is, in principle, free to add to $V_{1\pi}$ terms proportional to $E_{\vec{p}} - E_{\vec{p}'}$.

Because of parity conservation, the next-to-leading-order (NLO) corrections to the potential appear at order Q^2 rather than Q (2). For all two-pion exchange diagrams in **Figure 2** (except for the box graph in **Figure 2*e***), the potential can be defined via the identification $V_{2\pi}^{(2)} = T_{2\pi}^{(2)}|_{E_{\vec{p}}=E_{\vec{p}'}}$. In the case of the box diagram, we have to subtract the iterated one-pion exchange contribution $\hat{V}_{1\pi}^{(0)}\hat{G}_0\hat{V}_{1\pi}^{(0)}$ to avoid double counting. Evaluating the corresponding Feynman diagram in the CMS, one obtains a contribution proportional to the integral

$$\begin{aligned}&\int \frac{d^4l}{(2\pi)^4}\frac{(2m_N)^2 i}{[(p-l)^2 - m_N^2 + i\epsilon][(p+l)^2 - m_N^2 + i\epsilon][l_1^2 - M_\pi^2 + i\epsilon][l_2^2 - M_\pi^2 + i\epsilon]}\\ &= \int \frac{d^3l}{(2\pi)^3}\left(\frac{1}{\omega_1^2(E_{\vec{p}} - E_{\vec{p}-\vec{l}} + i\epsilon)\omega_2^2} + \frac{\omega_1^2+\omega_1\omega_2+\omega_2^2}{2\omega_1^3\omega_2^3(\omega_1+\omega_2)} + \mathcal{O}(m_N^{-1})\right),\end{aligned} \qquad 11.$$

where $\omega_i = \sqrt{\vec{l}^{\,2} + M_\pi^2}$ and the virtual pion momenta are given by $l_1 = l$ and $l_2 = l + q$. Note that we use here the relativistic expressions for the nucleon propagators in order to avoid the pinch singularity discussed in the previous section. The first term within the round brackets is nothing but the iterated one-pion exchange, $\hat{V}_{1\pi}^{(0)}\hat{G}_0\hat{V}_{1\pi}^{(0)}$, whereas the second one gives rise to $V_{2\pi,\mathrm{box}}^{(2)}$. Note further that, as explained above, the iterated one-pion exchange is enhanced, compared with the estimation $\sim Q^2$ based on naïve dimensional analysis, because $E \sim \mathcal{O}(Q^2/m_N) \ll \mathcal{O}(Q)$.

The final result for the two-pion exchange potential at order Q^2 can now be obtained by evaluating the loop integrals and carrying out the spin-isospin algebra. Employing dimensional regularization and using the decomposition

$$V = V_C + \boldsymbol{\tau}_1\cdot\boldsymbol{\tau}_2\, W_C + [V_S + \boldsymbol{\tau}_1\cdot\boldsymbol{\tau}_2\, W_S]\vec{\sigma}_1\cdot\vec{\sigma}_2 + [V_T + \boldsymbol{\tau}_1\cdot\boldsymbol{\tau}_2\, W_T]\vec{\sigma}_1\cdot\vec{q}\;\vec{\sigma}_2\cdot\vec{q}, \qquad 12.$$

it takes the form

$$W_C^{(2)} = -\frac{L(|\vec{q}|)}{384\pi^2 F_\pi^4}\left[4M_\pi^2(5g_A^4 - 4g_A^2 - 1) + \vec{q}^{\,2}(23g_A^4 - 10g_A^2 - 1) + \frac{48g_A^4 M_\pi^4}{4M_\pi^2 + \vec{q}^{\,2}}\right],$$
$$V_T^{(2)} = -\frac{1}{\vec{q}^{\,2}} V_S^{(2)} = -\frac{3g_A^4}{64\pi^2 F_\pi^4} L(|\vec{q}|), \qquad 13.$$

where we do not show the contributions that are polynomial in momenta because these can be absorbed into the contact interactions. The loop function L is defined via

$$L(|\vec{q}|) = \frac{\sqrt{4M_\pi^2 + \vec{q}^{\,2}}}{|\vec{q}|} \ln \frac{\sqrt{4M_\pi^2 + \vec{q}^{\,2}} + |\vec{q}|}{2M_\pi}. \qquad 14.$$

Note that the UV divergences entering the loop integrals are polynomial in the external momenta and, therefore, do not affect the nonpolynomial pieces if one uses dimensional regularization or equivalent schemes.

The N^{2}LO corrections emerge at order Q^3. Again, parity conservation forbids any one-pion exchange contributions at this order. The two-pion exchange terms emerge from the triangle diagram in **Figure 2*f*** through the identification $V_{2\pi}^{(3)} = T_{2\pi}^{(3)}|_{E_{\vec{p}}=E_{\vec{p}'}}$, whereas the diagram in **Figure 2*g*** yields a vanishing result. One finds that

$$V_C^{(3)} = -\frac{3g_A^2}{16\pi F_\pi^4}[2M_\pi^2(2c_1 - c_3) - c_3 q^2](2M_\pi^2 + q^2)A(|\vec{q}|),$$
$$W_T^{(3)} = -\frac{1}{q^2} W_S^{(3)} = -\frac{g_A^2}{32\pi F_\pi^4} c_4 (4M_\pi^2 + q^2) A(|\vec{q}|), \qquad 15.$$

where the c_i are LECs associated with the $\pi\pi NN$ vertices of order $\Delta_i = 1$ and the loop function A is given by

$$A(|\vec{q}|) = \frac{1}{2|\vec{q}|} \arctan \frac{|\vec{q}|}{2M_\pi}. \qquad 16.$$

In addition to the static terms, in principle there are also $1/m_N$ corrections to NLO graphs; see, for example, the last term within the brackets in Equation 11. The nucleon mass is, however, often treated as a very heavy scale with $m_N \gg \Lambda$ (see Reference 2 for a discussion), leading to a suppression of the $1/m_N$ corrections.

We now address the convergence of the chiral expansion for the long-range 2NF. Given that the obtained expressions depend solely on the momentum transfer $\vec{q}$, the potential is expected to be local in coordinate space,

$$V(\vec{r}) = \tilde{V}_C + \boldsymbol{\tau}_1 \cdot \boldsymbol{\tau}_2\, \tilde{W}_C + [\tilde{V}_S + \boldsymbol{\tau}_1 \cdot \boldsymbol{\tau}_2\, \tilde{W}_S]\vec{\sigma}_1 \cdot \vec{\sigma}_2 + [\tilde{V}_T + \boldsymbol{\tau}_1 \cdot \boldsymbol{\tau}_2\, \tilde{W}_T] S_{12}, \qquad 17.$$

where r is the distance between the nucleons, $S_{12} \equiv (3\vec{\sigma}_1 \cdot \vec{r}\,\vec{\sigma}_2 \cdot \vec{r} - \vec{\sigma}_1 \cdot \vec{\sigma}_2 r^2)/r^2$, and $\tilde{V}_X$ and $\tilde{W}_X$ are scalar functions of $r \equiv |\vec{r}|$. The Fourier transform of the expressions in Equations 13 and 15 is, however, ill defined because the potentials are not bounded as q increases, where $q \equiv |\vec{q}|$. At finite distances, $r > 0$, the potential can be obtained through a suitable regularization,

$$V(\vec{r}) = \lim_{\Lambda\to\infty} \int \frac{d^3q}{(2\pi)^3} e^{-i\vec{q}\cdot\vec{r}}\, V(\vec{q}) F_\Lambda(|\vec{q}|), \qquad 18.$$

where the regulator function $F_\Lambda(x)$ can be chosen as, for instance, $F_\Lambda(x) = \exp(-x^2/\Lambda^2)$. Alternatively, and more elegantly, one can write the functions W_X and V_X in terms of a continuous superposition of Yukawa functions that can easily be Fourier transformed (see Reference 19 for more details). For example, for central potentials one obtains the unsubtracted

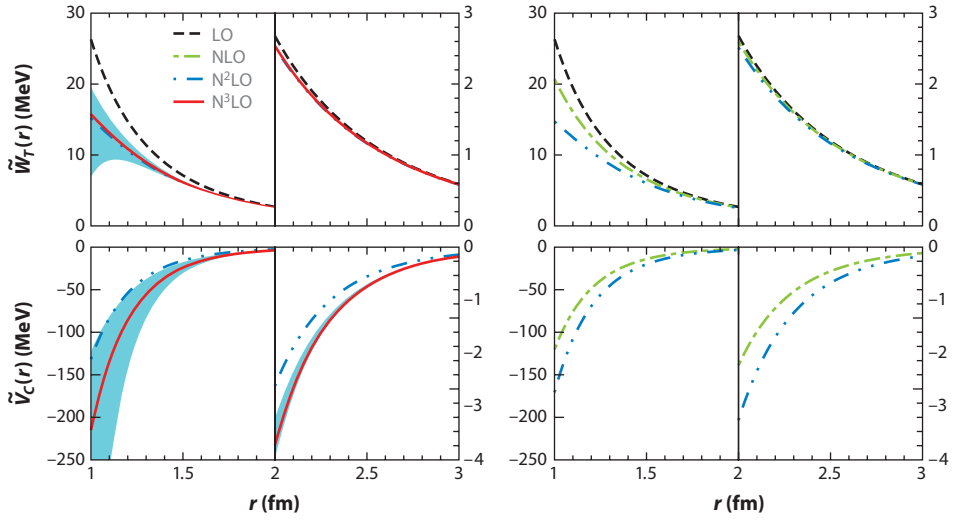

Figure 3

Chiral expansion of the isovector-tensor (*top row*) and isoscalar-central (*bottom row*) long-range potentials $\tilde{W}_T(r)$ and $\tilde{V}_C(r)$, respectively. The left (right) panels show the results for the effective field theory without (with) explicit $\Delta(1,232)$ degrees of freedom. The shaded bands represent the estimated scheme dependence, which is intrinsic to the separation between the long- and short-range contributions in the potential (shown only for the theory without Δs). Abbreviations: LO, leading order; NLO, next-to-leading order; N^2LO, next-to-next-to-leading order; N^3LO, next-to-next-to-next-to-leading order.

dispersive representation

$$V_C(q) = \frac{2}{\pi}\int_{2M_\pi}^{\infty} d\mu\ \mu \frac{\rho_C(\mu)}{\mu^2+q^2}, \quad V_C(r) = \frac{1}{2\pi^2 r}\int_{2M_\pi}^{\infty} d\mu\ \mu e^{-\mu r}\rho_C(\mu), \qquad 19.$$

where $\rho_C(\mu) = \text{Im}\,[V_C(0^+ - i\mu)]$ is the corresponding spectral function.

Figure 3 shows the chiral expansion for the two most important cases, specifically the isovector-tensor and isoscalar-central potentials $\tilde{W}_T(r)$ and $\tilde{V}_C(r)$. We also include the contributions at next-to-next-to-next-to-leading order (N^3LO), whose explicit form can be found in Reference 21; however, we restrict ourselves to the local pieces, omitting the $1/m_N$ corrections. We include in the dispersive integrals in Equation 19 only the components in the spectrum with $\mu < \tilde{\Lambda} = 1$ GeV. The high-μ components generate terms that, at low momenta, are indistinguishable from contact interactions parameterizing the short-range part of the chiral potential. The bands correspond to the variation of $\tilde{\Lambda}$ in the range from 800 MeV to ∞. Their widths may, therefore, serve as an estimation of the size of short-range components that are not associated with the dynamics of Goldstone bosons.

The potential in the isovector-tensor channel is clearly dominated by one-pion exchange, $V_{1\pi}$. Two-pion exchange contributions in this channel become visible at distances of the order $r \sim 2$ fm and shorter. The strong, attractive isoscalar-central potential in the intermediate range is another well-known feature of the 2NF. Phenomenologically, it is attributed to the correlated two-pion exchange, which is often modeled in terms of σ-meson exchange (22). In chiral EFT, however, all low-energy manifestations of the σ and other heavy mesons are systematically taken into account through values of the LECs in the effective Lagrangian. The resulting strength of $\tilde{V}_C$ is comparable to that of $V_{1\pi}$, even at distances $r \sim 2$ fm, and appears to be an order of magnitude larger than the strength of the two-pion exchange in any other channel. The large

size of the N^{2}LO contributions can be traced back to the large numerical factor of 3/16 in the case of $V_C^{(3)}$, an enhancement by one power of π (Equations 13 and 15), and the large values of the LECs $c_{3,4}$. For example, the determination from πN subthreshold coefficients at order Q^2 leads to $c_3 = -3.9$ GeV^{-1} and $c_4 = 2.9$ GeV^{-1} (23, 24), which are larger in magnitude than the expected natural size, $|c_{3,4}| \sim g_A/\Lambda \sim 1$ GeV^{-1}. Moreover, even larger values are obtained from πN scattering at order Q^3, where the effects of pion loops are taken into account (25, 26). The large values of $c_{3,4}$ can be traced back to the implicit treatment of the $\Delta(1,232)$ isobar. Given the fairly low excitation energy of the Δ ($m_\Delta - m_N$, which is numerically $\sim 2M_\pi$), one may expect that its explicit inclusion in the EFT within the so-called small-scale expansion (27), based on the (phenomenological) extension of the counting in Equation 2, to

$$\epsilon \in \left\{ \frac{M_\pi}{\Lambda}, \frac{|\vec{k}|}{\Lambda}, \frac{m_\Delta - m_N}{\Lambda} \right\} \qquad 20.$$

would allow one to resum a certain class of important contributions, leading to a superior convergence compared with the Δ-less theory. The improved convergence is indeed observed in the cases of both πN scattering (28) and nuclear forces (24, 29, 30). In particular, the dominant contribution to V_C and W_T has already emerged in the Δ-full theory at NLO; the N^{2}LO contributions provide fairly small corrections (**Figure 3**). For example, at NLO the single Δ excitation in **Figure 2*d,e***
generates the isoscalar-central potential

$$V_C^{(2)} = -\frac{g_A^2 h_A^2}{12\pi F_\pi^4 (m_\Delta - m_N)} (2M_\pi^2 + q^2)^2 A(|\vec{q}\,|), \qquad 21.$$

where h_A denotes the $\pi N\Delta$ axial coupling. In the standard Δ-less approach based on the assignment $m_\Delta - m_N \sim \Lambda \gg M_\pi$, this numerically large contribution is shifted to N^{2}LO, where it is reproduced through the Δ-isobar saturation of c_3, $c_3^\Delta = -4h_A^2/[9(m_\Delta - m_N)]$ (23); see Equation 15. Having explicitly included the effects of the Δ isobar, one finds strongly reduced values of the LECs $c_{3,4}$, which agrees with the naturalness assumption. For example, by using $h_A = 3g_A/(2\sqrt{2})$ from $SU(4)$ or large N_c, one obtains $c_3 = -0.8$ GeV^{-1} and $c_4 = 1.3$ GeV^{-1} (30). Thus, the major part of the unnaturally large subleading two-pion exchange potential at N^{2}LO is shifted to NLO in the Δ-full theory. **Figure 3** illustrates this more natural convergence pattern.

When substituted into the Schrödinger equation, the long-range potentials introduced above provide an approximate representation of the nearby left-hand singularities in the partial-wave amplitude shown in **Figure 1**. These potentials cause a rapid energy dependence and indicate nontrivial relations between the coefficients in the effective-range expansion that can be regarded as low-energy theorems (LETs) (31–33) and confronted with the data. A pedagogical introduction to the LETs and their relation to the so-called modified effective range expansion can be found in Reference 34. Assuming that the pion exchange contributions are perturbative, these relations can be worked out analytically within the scheme proposed by Kaplan et al. (35). The resulting LETs, however, appear to be strongly violated in the $^1S_0$ and $^3S_1$–$^3D_1$ channels (31, 32). This observation indicates the nonperturbative nature of the one-pion exchange potential, at least in these channels (36). By employing a nonperturbative treatment of the pion exchange potential, Epelbaum et al. (37) tested the LETs numerically. Birse and collaborators (38–41) followed a closely related approach by analyzing the energy dependence of the residual short-range potential in a given partial wave. Perhaps the most impressive evidence of the chiral two-pion exchange comes from the Nijmegen partial-wave analysis of proton-proton (*pp*) scattering (42), where the Schrödinger equation was solved for a specific choice of the long-range potential outside of some boundary b. The authors took short-range physics into account by choosing appropriate boundary conditions at $r = b$. The number of parameters needed to describe experimental data

below the pion production threshold with χ^2/datum ~ 1 can be regarded as a measure of the amount of physics not included in the long-range potential. By using $b = 1.4$ fm, the authors of Reference 42 observed a reduction ($31 \to 28 \to 23$) in the number of parameters when they employed $V_{1\pi} \to V_{1\pi} + V_{2\pi}^{(2)} \to V_{1\pi} + V_{2\pi}^{(2)} + V_{2\pi}^{(3)}$ as the long-range potential (in addition to the corresponding electromagnetic interactions).

2.3. Nuclear Forces: Status and Open Issues

We now summarize the current status of the nuclear forces within the heavy-baryon, Δ-less formulation based on the power counting of Equation 4. In this scheme, the nuclear Hamiltonian is presently worked out up to N^{3}LO in the chiral expansion,

$$H = H_0 + V_{2N} + V_{3N} + V_{4N} + \cdots, \qquad 22.$$

with

$$\begin{aligned} V_{2N} &= V_{2N}^{(0)} + V_{2N}^{(2)} + V_{2N}^{(3)} + V_{2N}^{(4)} + \cdots, \\ V_{3N} &= V_{3N}^{(3)} + V_{3N}^{(4)} + \cdots, \\ V_{4N} &= V_{4N}^{(4)} + \cdots, \end{aligned} \qquad 23.$$

where the ellipses refer to terms beyond N^{3}LO. For two nucleons, it is necessary and sufficient to go to N^{3}LO to accurately describe the *np* and *pp* phase shifts up to laboratory energies of $E_{\rm lab} \sim 200$ MeV (37, 43). This scenario is shown in **Figure 4**, where, as a representative example, the experimental data for the *np* differential cross section and vector analyzing power at $E_{\rm lab} = 50$ MeV are compared with calculations based on the chiral *NN* potentials from References 37 and 43, as well as various modern phenomenological potentials. At N^{3}LO accuracy, it is mandatory to take into account isospin-breaking (IB) contributions. The dominant IB effects emerge from the charged-to-neutral-pion mass difference in the one- and two-pion exchange (charge-independence breaking) (46), the proton-to-neutron mass difference in the two-pion exchange (charge-symmetry breaking) (47, 48), and the two derivative-less contact interactions (both charge-independence and charge-symmetry breaking in the two *S*-waves). The short-range part of the potential at N^{3}LO receives contributions from 24 isospin-invariant and 2 IB contact interactions whose strength

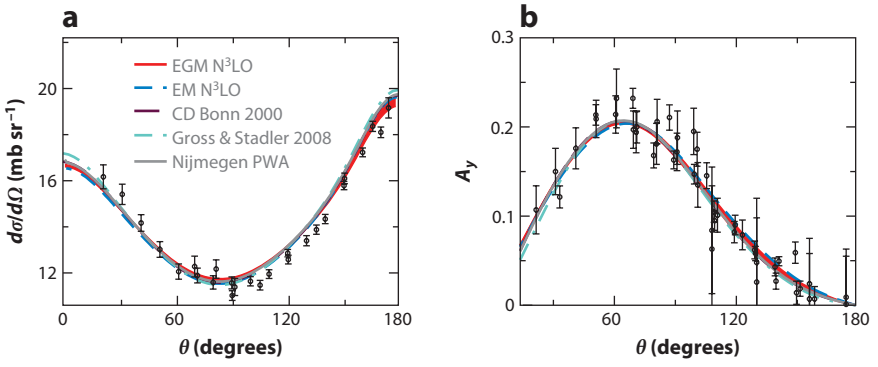

Figure 4

(*a*) Neutron-proton differential cross section and (*b*) analyzing power at $E_{\rm lab} = 50$ MeV, calculated by use of the chiral effective field theory, the CD Bonn 2000 potential (44), and the potential developed by Gross & Stadler (45). Also shown are results from the Nijmegen partial-wave analysis (PWA). References to data can be found at **http://nn-online.org**. EGM and EM refer to the potentials constructed by Epelbaum, Glöckle & Meißner and by Entem & Machleidt in References 37 and 43, respectively.

was adjusted to phase shifts (scattering data) in Reference 37 (43). Both available versions of the N^{3}LO potential employ a finite momentum-space cutoff to regularize the Schrödinger equation. This cutoff is varied in Reference 37 in the range $\Lambda = 450$–600 MeV. More details about the construction of chiral potentials at N^{3}LO can be found in two comprehensive review articles (7, 49).

Although the chiral expansion of the long-range nuclear forces emerges rather straightforwardly, the power counting for the short-range operators and the closely related issue of nonperturbative renormalization of the Schrödinger (or LS) equation are still being debated in the community (e.g., References 50–52). Here, the main conceptual difficulty is associated with the nonperturbative treatment of the one-pion exchange potential $V_{1\pi}$. Despite considerable efforts, (35, 53), no approximation to $V_{1\pi}$ is presently known that would capture the relevant nonperturbative physics and, at the same time, be analytically resummable and renormalizable. Therefore, one is left with the numerical solution of the Schrödinger equation for appropriately regularized chiral potentials, along the lines of the analysis in Reference 54. That paper also explains the meaning of renormalization in such an approach and provides a tool to verify its consistency a posteriori by means of the so-called Lepage plots. Note that iterating the potential, truncated at a given order of the chiral expansion, in the LS equation necessarily generates higher-order contributions in the amplitude that are generally UV divergent; renormalization of these contributions requires counterterms beyond the truncated potential. Therefore, in such an approach it is not legitimate to arbitrarily increase the cutoff Λ. This point is exemplified in Reference 33 through the use of an exactly solvable analytical model (also see Reference 54 for a qualitative discussion). More work is needed to (better) understand the power counting for the scattering amplitude in the presence of the long-range pion exchange potentials. A promising tool to address this question is provided by the modified effective range expansion (see the discussion in Reference 55, and see References 39 and 40 for related work). Also, it remains to be determined whether the renormalization group–based approach such as that proposed in Reference 56 can shed new light on this issue.

3NFs are an old but still relevant topic in nuclear physics. Despite many decades of effort, the detailed structure of the 3NF has not been captured by modern phenomenological 3NF models. Indeed, the global analysis presented in Reference 57 demonstrates that the available models do not allow one to significantly reduce the observed discrepancies between the experimental data and calculations based on the high-precision *NN* potentials for breakup and polarization observables in elastic nucleon-deuteron (*Nd*) scattering. Given the very rich spin-momentum structure of the 3NF compared with that of the *NN* force, the more sparse database in the three-nucleon sector, and the relatively high computational cost of solving the Faddeev equation, further progress in this field clearly requires input from theory. This situation provides a strong motivation to study the structure of the 3NF within chiral EFT.

The general structure of the 3NF up to order Q^4, which also holds at order Q^5, is represented by six topologies (**Figure 5**). The first nonvanishing contributions emerge at N^{2}LO (Q^3) (58, 59) from the two-pion (**Figure 5*a***), one-pion contact (**Figure 5*d***) and contact (**Figure 5*f***) diagrams. The corresponding πN ($\pi\pi N$, πNN, NNN) amplitudes at this order are given simply by the $\Delta_i = 0$ ($\Delta_i = 1$) vertices from the effective Lagrangian. The one-pion contact and contact diagrams depend on the two LECs c_D and c_E, respectively, whose determination requires few-nucleon data. We discuss the applications of the resulting nuclear Hamiltonian to the properties of few-nucleon systems in the next section. Note, however, that the leading 3NF involves a rather restricted set of isospin-spin-momentum structures, which are also included in the phenomenological 3NF models. In particular, the longest-range two-pion exchange topology (**Figure 5*a***) is well established as one of the most important phenomenological 3NF mechanisms. The leading chiral 3NF cannot,

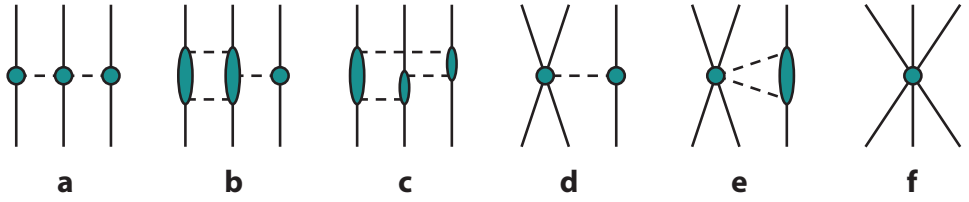

Figure 5

(*a–f*) Various topologies contributing to the three-nucleon force up to order Q^5. Shaded areas represent the corresponding amplitudes.

therefore, be expected to shed new light on the persistent deficiencies in the theoretical description of, for instance, *Nd* scattering. The corrections to the 3NF at N^{3}LO generated by the leading-loop diagrams are performed in References 60–62. Remarkably, the N^{3}LO terms do not involve any unknown LECs. In addition to the static loop contributions, one also has to take into account the $1/m_N$ corrections in the topologies in **Figure 5*a*** and ***d*** (62; also see the earlier calculation in Reference 63). The numerical implementation of the novel N^{3}LO contributions in few-body studies is nontrivial and requires a partial-wave decomposition. This work is presently in progress; see Reference 64 for an initial step in this direction.

Clearly, one of the most interesting features of the 3NF at N^{3}LO is its rich spin-momentum structure, which yields many operators that have never been explored in few-body studies and could be capable of resolving the observed discrepancies in three-nucleon scattering. This feature especially applies to the ring topology in **Figure 5*c*** and, to a lesser extent, the two-pion/one-pion topology in **Figure 5*b***. However, the observed convergence pattern of the chiral expansion of the two-pion exchange two-nucleon potential with the diagrams in **Figure 2*b–e*** yields small contributions, and the major effect that emerges from the subleading diagram in **Figure 2*f*** (see the previous section) brings the convergence of the 3NF at N^{3}LO into question. Indeed, because the (large) LECs $c_{2,3,4}$ saturated by the Δ isobar do not contribute to the ring and two-pion/one-pion exchange 3NF topologies at N^{3}LO, one may expect that the corresponding potentials from Reference 61 have not yet converged (also see the discussion in Reference 65). Thus, one may either need to go to at least N^{4}LO in the Δ-less theory or explicitly take into account the contributions of the Δ isobar up to N^{3}LO. Such work is in progress; see Reference 66 for the first steps in this research.

The parameter-free results that are currently being and have been obtained in chiral EFT for the various components of the 3NF at large distances rely solely on the spontaneously broken chiral symmetry of QCD. These results introduce a very interesting possibility for benchmarking with future lattice QCD calculations[3] (see References 67 and 68 for the initial efforts).

Finally, the 4NF also receives its first contribution at N^{3}LO from tree-level diagrams constructed from the lowest-order vertices of dimension $\Delta_i = 0$. The parameter-free expressions for the 4NF at N^{3}LO can be found in Reference 18. The contribution of the 4NF to the α-particle binding energy (BE) was estimated (69) to be of the order of a few hundred keV. This value provides some justification for neglect of four (and more)-nucleon forces in nuclear structure calculations.

[3] Clearly, one must take care when dealing with the nonuniqueness of the nuclear potentials. The long-range part of the 3NF at N^{3}LO is, however, uniquely determined after fixing the corresponding long-range part of the 2NF.

3. APPLICATIONS TO FEW-NUCLEON SYSTEMS

Having determined most of the parameters in the nuclear Hamiltonian from *NN* data, it is now interesting to test them in few-nucleon reactions in which the A-nucleon Schrödinger equation (Equation 1) can be exactly solved numerically. For three particles, the Schrödinger equation can be conveniently rewritten in terms of the Faddeev integral equations, which are usually solved in the partial-wave basis (see Reference 70 for details). The Faddeev equations can be routinely solved for any given two- and three-nucleon potentials for both bound and scattering states. For a review of recent progress toward including the Coulomb interaction in three-nucleon scattering, see Reference 71.

As explained in the previous section, the 3NF at N^2LO depends on two LECs, c_D and c_E, which need to be determined from few-nucleon data. In Reference 59, c_D and c_E were tuned to the triton BE and the neutron-deuteron (*nd*) doublet scattering length. The resulting parameter-free nuclear Hamiltonian was then tested in *Nd* scattering. **Figure 6** compares a sample of results with the data. The bands emerge from the cutoff variation, as discussed in the previous section. Note

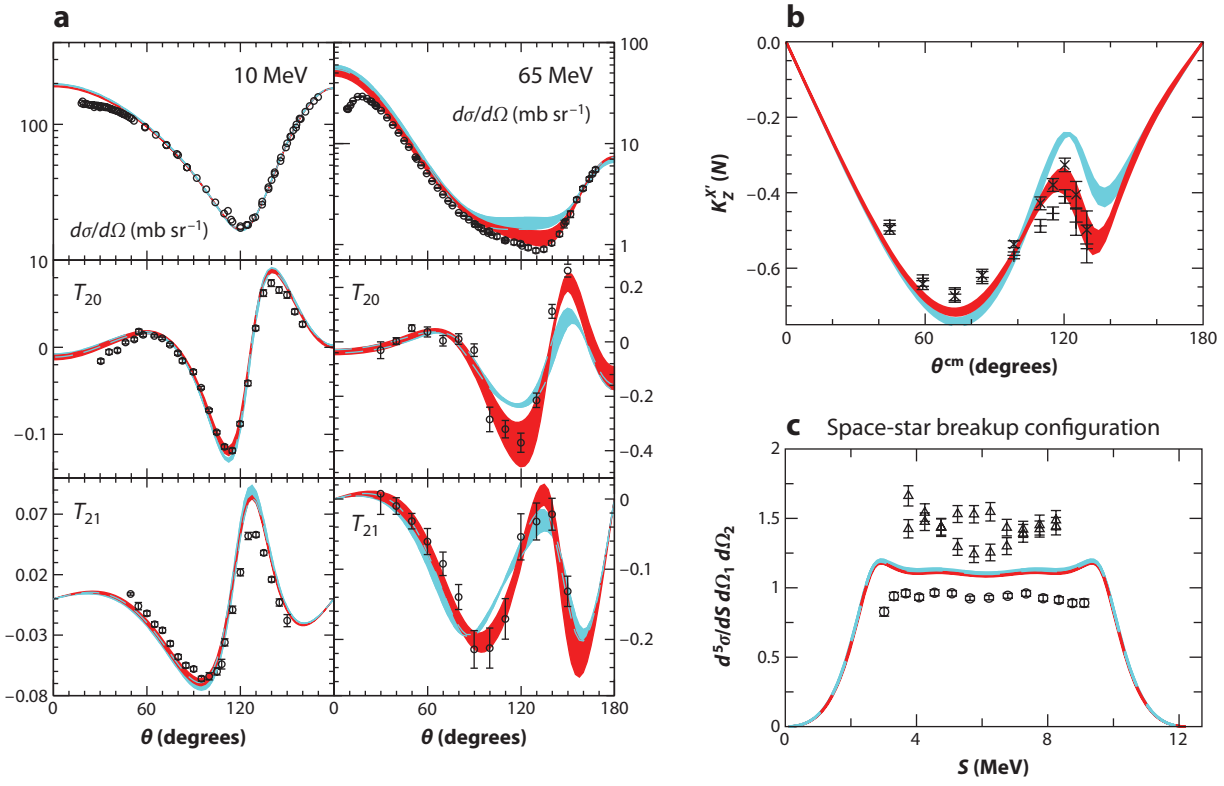

Figure 6

(*a*) Differential cross section and tensor analyzing powers T_{20} and T_{21} for elastic nucleon-deuteron (*Nd*) scattering at $E_{\rm lab}^N = 10$ and 65 MeV. (*b*) The nucleon-to-nucleon polarization transfer coefficient in elastic *Nd* scattering at $E_{\rm lab}^N = 22.7$ MeV [the proton-deuteron (*pd*) data are from Reference 72]. (*c*) *Nd* breakup cross section in the space-star configuration (upper sets of data, *nd*; lower sets of data, *pd*). The blue and red shaded bands show the results from the chiral effective field theory at next-to-leading order and next-to-next-to-leading order, in order. The precise kinematical description and references to data can be found in Reference 70.

that the NLO results are based solely on the 2NF. We further emphasize that the calculations shown do not include the Coulomb interaction and thus correspond to *nd* scattering. We have corrected the proton-deuteron data at $E_{\rm lab}^N = 10$ MeV by subtracting out the (estimated) Coulomb-force contribution (see Reference 59 for additional details). Remarkably, even some accurate data for double-polarization observables are available at low energy. As a representative example, **Figure 6*b*** shows our results for the nucleon-to-nucleon polarization transfer coefficient $K_z^{x'}(N)$ at $E_{\rm lab}^N = 22.7$ MeV, compared with data from Reference 72. Additional results for different polarization transfer coefficients at this energy, also based on conventional nuclear potentials, can be found in Reference 73. For most of the elastic observables, one can obtain an improved description when going from NLO to N^{2}LO, which is consistent with the description of two-nucleon data at these orders. The increasing theoretical uncertainty, however, limits the applicability of the N^{2}LO chiral forces to energies below $E_{\rm lab}^N \sim 100$ MeV, where the modern phenomenological 2NFs and 3NFs also provide an accurate description of the data. There is one well-known exception from the generally good agreement between the theory and the data at very low energies; this exception is known as the A_y puzzle. It refers to the strong underprediction of the nucleon vector analyzing power observed at energies below $E_{\rm lab}^N \sim 30$ MeV for all modern two- and three-nucleon potentials; see Reference 70 for more details. We emphasize, however, that A_y is (*a*) very small at these energies and (*b*) very sensitive to small contributions to the nuclear force (70); see Reference 57 for an extensive discussion. Therefore, it is not surprising that the solution to the A_y puzzle in chiral EFT has not been achieved at N^{2}LO and requires the inclusion of higher-order terms in the Hamiltonian.

The kinematically very rich deuteron breakup reactions provide even more detailed insights into nuclear dynamics. At low energies, only a very few selected observables, mainly the cross section, are available in certain regions of the phase space. Although good agreement between the data and calculations based on the conventional potentials and chiral EFT has been observed for the final-state-interaction and quasi-free-scattering configurations, large discrepancies occur in the case of the space-star configuration (the plane in the CMS spanned by the outgoing nucleons is perpendicular to the beam axis, and the angles between the nucleons are 120°). This discrepancy is shown in **Figure 6*c*** (compare with the upper sets of *nd* data). Remarkably, the existing 3NFs have almost no effect on this observable. For recent studies of related breakup configurations, see References 74 and 75.

At higher energies, the situation is similar to the one in the elastic channels; the predictions from chiral EFT generally agree with the data but show a rapidly increasing theoretical uncertainty. See References 76–78, which compare the high-precision cross section and analyzing powers, measured recently at KVI at $E_{\rm lab}^N = 65$ MeV and covering a large part of the available phase space, with theoretical calculations. For a detailed review on three-nucleon scattering at intermediate energies, see Reference 57.

The four-nucleon continuum provides another interesting and (given the appearance of low-energy resonance structures) very sensitive testing ground for nuclear dynamics. It also offers the possibility of probing isospin channels that are not accessible in *Nd* scattering. The solution of the Schrödinger equation for four-nucleon scattering states still represents a major challenge, so only a restricted set of calculations, typically at low energies, is available. Interestingly, the A_y puzzle persists in the four-nucleon system, in which it becomes even more striking due to a much larger magnitude of A_y. The very recent study by the Pisa group (79) shows that, in contrast to the three-nucleon system, the A_y puzzle in the four-nucleon system is significantly reduced by inclusion of the chiral 3NF at N^{2}LO once the LECs c_D and c_E are adjusted to the ^{3}H and ^{4}He BEs. Given space constraints, we refrain from presenting a more detailed discussion of four-nucleon scattering and refer the reader to the review article (79).

The nuclear Hamiltonian at N^{2}LO has also been used to compute the spectra of light nuclei, yielding 7.7–8.5 MeV and 24.4–28.8 MeV for the triton and α-particle BEs, respectively, at NLO. These results agree well with the experimental values of 8.482 MeV and 28.30 MeV, respectively. When the triton BE is used as input in the determination of c_D and c_E, the α-particle BE at N^{2}LO, 27.8–28.6 MeV, is improved compared with its NLO value.

In all the applications discussed so far, the LECs entering the 3NF were determined from the triton BE and the *nd* scattering length. Given the strong correlation between these two observables, which is known as the Philips line and is caused by the large *S*-wave scattering lengths in the two-nucleon system, the resulting values for c_D and c_E suffer from a sizable uncertainty. Other possible ways to determine these LECs include fitting to the triton and α-particle BEs (80) or to the properties of light nuclei (81). Recently, Gazit et al. (82) exploited the fact that the LEC c_D not only contributes to the 3NF at N^{2}LO but also governs the strength of the dominant short-range axial vector exchange current to find that c_D can be determined from weak processes. By using the N^{3}LO 2NF from Reference 43, combined with the N^{2}LO 3NF in which c_D and c_E are calibrated to the triton BE and half-life, Gazit et al. (82) obtained an α-particle BE of 28.50(2) MeV. Also, these authors determined the point-proton radii of ^{3}H, ^{3}He, and ^{4}He to be 1.605(5) fm, 1.786(5) fm, and 1.461(2) fm, which are in excellent agreement with the corresponding experimental values of 1.60 fm, 1.77 fm, and 1.467(13) fm, respectively. These results provide an important and highly nontrivial consistency check of the chiral EFT approach by bridging the strong and axial few-nucleon processes.

Last but not least, the chiral 3NF at N^{2}LO has also been extensively explored in connection with the spectra of light and medium-mass nuclei; see References 83 and 84 for a recent review describing state-of-the-art calculations within the no-core-shell model and the limit of neutron-rich nuclei. Other recently covered topics include oxygen isotopes (85), the properties of nuclear matter and constraints on neutron star radii (86), the puzzle of the anomalously long β-decay lifetime of ^{14}C (87), and an ab initio coupled-cluster approach to nuclear structure (88).

4. NUCLEAR LATTICE SIMULATIONS

A novel scheme to tackle the nuclear A-body problem that combines chiral EFT for nuclear forces with Monte Carlo (MC) methods, which have been successfully used in lattice QCD and other fields of physics, consists of the so-called nuclear lattice simulations, collectively known as nuclear lattice EFT (NLEFT). Below, we give a brief outline of this approach and present some early results (for a review with many references to earlier, related work, see Reference 89).

4.1. Formalism

In NLEFT, space-time is discretized in Euclidean time on a torus of volume $L_s \times L_s \times L_s \times L_t$, where L_s (L_t) is the side length in the spatial (temporal) direction (**Figure 7**). The minimal distance on the lattice, the so-called lattice spacing, is a (a_t) in space (time). This distance entails a maximum momentum on the lattice, $p_{\max} = \pi/a$, which serves as a UV regulator of the theory. In contrast to lattice QCD, we do not take the continuum limit $a \to 0$ because we are dealing with an EFT and do not wish to resolve the structure of individual nucleons. The nucleons are treated as point-like particles residing on the lattice sites, whereas the nuclear interactions (pion exchanges and contact terms) are represented as insertions on the nucleon world lines by use of standard auxiliary field representations. The nuclear forces have an approximate spin-isospin $SU(4)$ symmetry (Wigner symmetry) (90) that is of fundamental importance in suppressing the malicious sign oscillations that plague any MC simulation of strongly interacting fermion systems at finite density (for

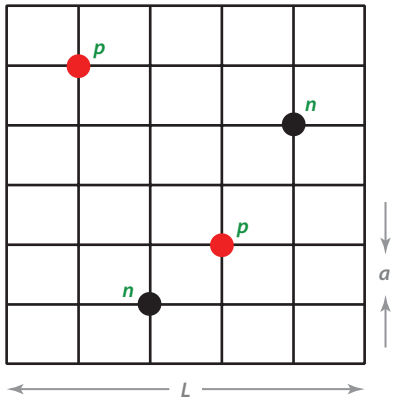

Figure 7

Schematic illustration of the space-time lattice. The minimal length is the lattice spacing a. The side length L in any spatial direction is an integer multiple of a. Protons (p) and neutrons (n) reside on the lattice sites.

a modern look at this symmetry, see Reference 91). The derivation of inequalities for BEs of light nuclei in the Wigner symmetry limit is given in Reference 92. Because of this approximate symmetry, nuclear lattice simulations provide access to a large part of the phase diagram of QCD (**Figure 8**), whereas calculations using lattice QCD are limited to finite temperatures and low densities (baryon chemical potential). Here, we concentrate on calculations of the ground-state properties and the excited states of atomic nuclei with $A \leq 12$.

We have simulated the interactions of nucleons by using the MC transfer matrix projection method (5). Each nucleon evolves as if it were a single particle in a fluctuating background of

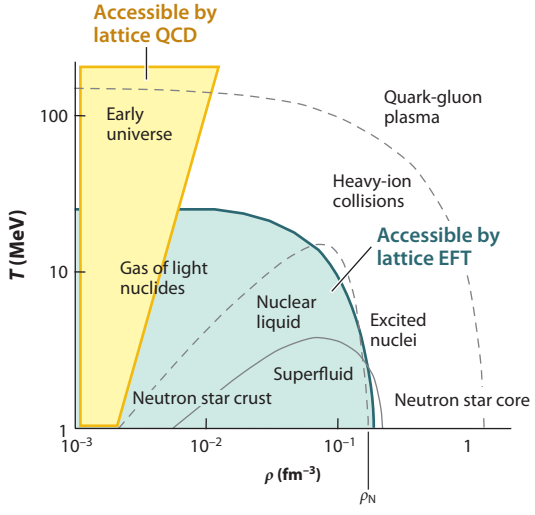

Figure 8

Nuclear phase diagram as accessible by lattice quantum chromodynamics (QCD) (*yellow area*) and by nuclear lattice effective field theory (EFT) (*blue-gray area*). On the abscissa, the nuclear density ρ (where ρ_N is the density of nuclear matter) is shown. On the ordinate, the temperature T is displayed. Figure reproduced courtesy of Dean Lee.

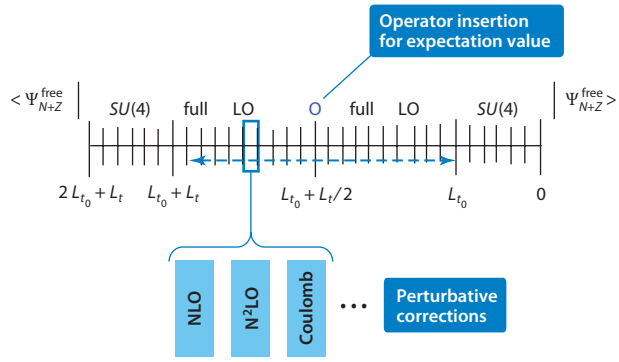

Figure 9

Schematic representation of the transfer matrix calculation. For the first t_0 time steps, the $SU(4)$ symmetric part of the leading-order (LO) action is employed, which serves as an inexpensive filter to suppress the sign oscillations. Only then is the full LO action used. All higher-order corrections are included perturbatively, as shown. The initial and final wave functions are a Slater determinant of Z protons and N neutrons. Abbreviations: NLO, next-to-leading order; N^2LO, next-to-next-to-leading order.

pion and auxiliary fields; the latter represent the multinucleon contact interactions (for detailed definitions at LO in the chiral expansion, see Reference 93). We have also performed Gaussian smearing of the LO contact interactions, which is required by the too strong binding of four nucleons on one lattice site. More precisely, in a LO calculation that uses the two independent four-nucleon contact operators without derivatives, $\sim (N^\dagger N)^2$, the ground state of the ^{4}He system is severely overbound and consists almost entirely of the quantum state where all four nucleons occupy the same lattice site. This situation arises in part from a combinatorial enhancement of the contact interactions when more than two nucleons occupy the same lattice site. This effect can be partly overcome by higher-order four-nucleon operators, but it is most efficiently dealt with by use of a Gaussian smearing procedure, which turns the point-like vertex into an extended structure. A detailed discussion of this issue can be found in Reference 93. Remarkably, the aforementioned configurations have led to a new interpretation of the phenomenon of clustering in nuclei (94).

Let us return to the simulation method. To LO, we begin with a Slater determinant of single-nucleon standing waves in a periodic cube for Z protons and N neutrons (where $Z + N = A$). We use the $SU(4)$ symmetric approximation of the LO interaction as an approximate inexpensive filter for the first t_0 time steps, which dramatically suppresses the sign oscillations. Then we switch on the full LO interaction and calculate the ground-state energy and other properties from the correlation function

$$Z_A(t) = \langle \Psi_A | \exp(-tH) | \Psi_A \rangle, \qquad 24.$$

letting the Euclidean time t go to infinity. Here, Ψ_A is the Slater-type initial wave function and H is the nuclear Hamiltonian, expressed in terms of the lattice variables and lattice fields. Higher-order contributions, namely the Coulomb repulsion between protons and other IB effects (due to the light quark mass difference), are computed as perturbative corrections to the LO transfer matrix (**Figure 9**). The perturbative treatment of all these effects is justified as for typical lattice spacings of $a \simeq 2$ fm; the maximal momentum is $p_{max} \simeq 300$ MeV. Note, however, that due to the Gaussian smearing of the LO contact interactions, a part of the higher-order corrections is also treated nonperturbatively. If one is interested in the expectation value of any operator $\mathcal{O}$, Equation 24 has to be generalized to

$$Z_A^{\mathcal{O}} = \langle \Psi_A | \exp(-tH/2) \mathcal{O} \exp(-tH/2) | \Psi_A \rangle, \qquad 25.$$

and the ground-state expectation value is obtained as the Euclidean time goes to infinity (**Figure 9**). Excited states are calculated from a multichannel projection MC method (95). As a first step, we use various improvements in our LO lattice action. This step is necessary to suppress, as much as possible, the artifacts from the lattice so that the rotational symmetry $SO(3)$ is broken to cubic symmetry $SO(3, Z)$ and further artifacts due to the finite lattice spacing a arise. To minimize the effect of these artifacts, one performs $\mathcal{O}(a^4)$ improvements for the nucleon kinetic energy and the Gaussian smearing factors of the contact interactions. Moreover, all lattice operators at $\mathcal{O}(Q^3)$ are included, in particular those related to the breaking of rotational symmetry. Their strengths can be tuned to eliminate unphysical partial-wave mixing such as that, for instance, between the ${}^3S_1 - {}^3D_1$ and ${}^3D_3$ partial waves. One then uses a set of Slater determinants of numerous single-nucleon standing waves; for example, for the calculation of the spectrum of ^{12}C, 24 initial standing waves were used, and from these, three states with a total momentum of zero and $J_z = 0 \bmod 4$ and one state with $J_z = 2 \bmod 4$ were constructed. Therefore, the correlation function becomes a matrix:

$$Z_{\mathrm{A}}^{ij}(t) = \langle \Psi_{\mathrm{A}}^{i} | \exp(-tH) | \Psi_{\mathrm{A}}^{j} \rangle. \qquad 26.$$

Diagonalization of this matrix of a given ensemble of states with the required quantum numbers leads to a tower of states. One can thereby reconstruct the excitation spectrum of any given nucleus. However, due to the required computing resources, so far only the ground state and a few excited states for some nuclei have been computed.

The very low memory and trivially parallel structure of the lattice MC codes allow one to perform simulations that scale ideally with several thousand processors. The computational time scales with the number of nucleons A as $\mathrm{A}^{1.7}$ at fixed volume V and with $V^{1.5}$ for fixed A. The average sign, which is a measure of the severity of the sign oscillations, scales approximately as $\exp(-0.1\mathrm{A})$. Taking the calculation of ^{12}C as a benchmark, the required CPU time for a nucleus with spin S and isospin I can be estimated as

$$X^{\mathrm{CPU}} \approx X_{^{12}\mathrm{C}}^{\mathrm{CPU}} \times \left(\frac{\mathrm{A}}{12}\right)^{3.2} \exp[0.1(\mathrm{A}-12) + 3(S \bmod 2) + 4I], \qquad 27.$$

and the memory requirements to store the generated configurations are

$$X^{\mathrm{storage}} \approx X_{^{12}\mathrm{C}}^{\mathrm{storage}} \times \left(\frac{\mathrm{A}}{12}\right)^{2} \exp[0.1(\mathrm{A}-12) + 3(S \bmod 2) + 4I]. \qquad 28.$$

Therefore, combining high-performance computing with the forces derived from chiral EFT, and fixing the parameters in few-nucleon systems, permits true ab initio calculations of atomic nuclei and their structure, with a quantifiable uncertainty of any observable under investigation. Before we present the early results based on NLEFT, we emphasize the differences between this approach and other ab initio methods. One distinction is that in NLEFT all systematic errors are introduced up front when defining the low-energy EFT, which eliminates unknown approximation errors related to specific calculational tools, physical systems, or observables. By including higher-order interactions, one can expect a systematic improvement in all the low-energy observables. Another difference is that many different phenomena can be studied through the use of the same lattice action. Once the action is determined, it can be used to calculate bound nuclei, the ground state of neutron matter, or thermodynamic properties at nonzero temperature. In addition, NLEFT uses several efficient lattice methods that were developed for lattice QCD and condensed matter simulations, including Markov chain MC techniques, auxiliary fields (96, 97), pseudofermion methods (98), and nonlocal updating schemes such as hybrid MC (99–101).

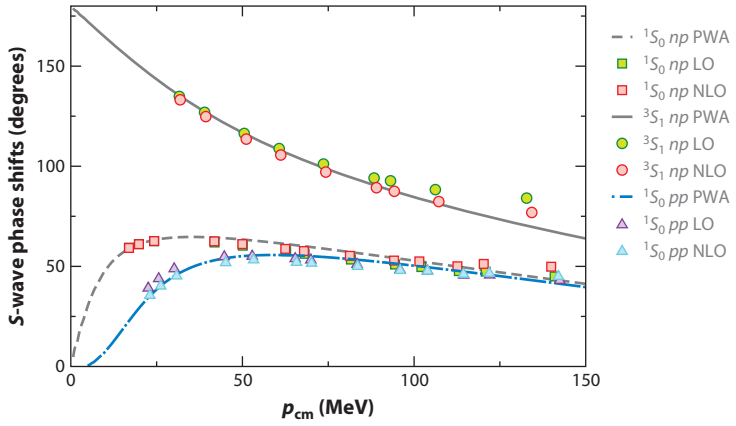

Figure 10

S-wave phase shifts in the two-nucleon system. From top to bottom: $^3S_1$ neutron-proton (*np*) scattering, $^1S_0$ *np* scattering, and $^1S_0$ proton-proton (*pp*) scattering. The open and filled symbols represent the results at leading order (LO) and next-to-leading order (NLO) (including all isospin-breaking effects), respectively. The curves are the result of the Nijmegen partial-wave analysis (PWA). Whereas the *np* phases are fitted, for the *pp* phase only the *pp* scattering length is input.

4.2. Results

So far, calculations in NLEFT have been performed up to N^{2}LO in the chiral expansion of the nuclear potential. At this order, both the two-body and leading three-body forces are present. First, consider the two-nucleon system. At NLO, nine parameters are determined from a fit to the *S*- and *P*-waves in *np* scattering. Two further IB parameters are determined from the *pp* and *nn* scattering lengths (102). Up to CMS momenta of the order of the pion mass, the empirical phase shifts in the *np* system have been well described (**Figure 10**), and furthermore, the NLO corrections are small. For these results to be obtained, a novel method to extract phase shifts from finite-volume simulations had to be developed (given that the standard Lüscher scheme is not well suited to this purpose in the case of strong partial-wave mixing) (104). Note that, due to the perturbative treatment of the higher-order effects, there are no contributions to the 2NF at N^{2}LO. The 3NF features only two LECs (Section 2.3); in our simulations, these LECs have been determined from the triton BE in combination with either low-energy *nd* scattering in the doublet channel (103) or the α-particle BE (95).

The first nontrivial predictions are (*a*) the energy dependence of the *pp* $^1S_0$ partial wave, which agrees with the Nijmegen partial-wave analysis up to momenta of approximately the pion mass (**Figure 10**), and (*b*) the BE difference between the triton (^{3}H) and ^{3}He,

$$E(^3\mathrm{He}) - E(^3\mathrm{H}) = 0.78(5)\ \mathrm{MeV}, \qquad 29.$$

which agrees well with the experimental value of 0.76 MeV (105, 106). The theoretical uncertainty arises primarily from the infinite-volume extrapolation. The following finite-volume expression has been utilized to arrive at the result for the three-nucleon ground-state energies:

$$E(L) = -\mathrm{BE} - \frac{a}{L}\exp(-bL). \qquad 30.$$

Here, BE is the positive binding energy, $E(L)$ is the measured energy in the finite volume L^3, and a and b are fit parameters (also see Reference 107).

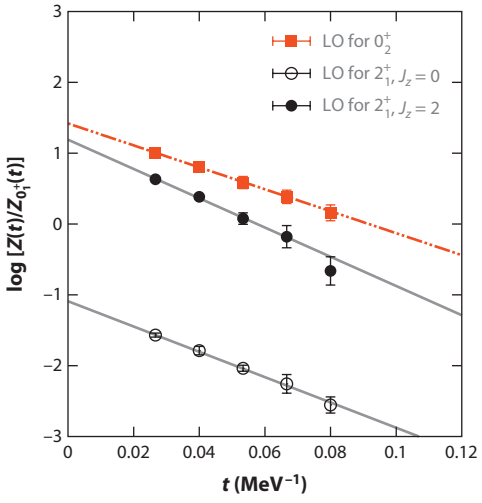

Figure 11

Extraction of the excited states of ^{12}C from the Euclidean time dependence of the projection amplitude at leading order (LO). The slope of the logarithm of $Z(t)/Z_{0_1^+}(t)$ at large t determines the energy relative to the ground state.

The ground-state energies of nuclei with A = 4, 6, or 12 were calculated in References 105 and 106, which showed that at N^{2}LO one can achieve a precision of a few percent. By refining the underlying action as described above and utilizing the multichannel projection MC method, Epelbaum et al. (95) determined the spectrum of ^{12}C. **Figure 11** shows the clean signals of the first few excited states on top of the 0^+ ground state. Note that due to lattice artifacts, the first excited 2^+ state is indeed split into two states. This problem will eventually be overcome through the choice of a larger basis of initial states.

In addition to the ground state and the excited spin-two state, the calculation predicts a resonance with an angular momentum of zero and positive parity at −85(3) MeV, very close to the ^{4}He+^{8}Be threshold at −86(2) MeV. Experimentally, this threshold is located at −84.80 MeV. This first 0^+ excitation is the so-called Hoyle state. It plays a crucial role in the helium burning of stars that are heavier than our Sun and in the production of carbon and other elements necessary for life. Hoyle (108) postulated that this excited state of ^{12}C was necessary for the fusion of three α-particles to produce a sufficient amount of carbon and other elements needed for life at stellar temperatures. For this reason, the Hoyle state plays a very important role in the context of the anthropic principle, although such considerations did not play any role when this state was predicted (109). The Hoyle state has been an enigma in nuclear structure theory for decades; even the most successful Green's function MC methods based on realistic 2NFs and 3NFs (110) or the no-core-shell model employing modern (chiral or $V_{\text{low-}k}$) interactions (81, 83) were unable to describe this state. **Table 1** shows results for the ground state and the low-lying excited states of ^{12}C at LO, NLO (with IB and electromagnetic corrections included), and N^{2}LO. For comparison, we list the experimentally observed energies.

The N^{2}LO results for the Hoyle state and spin-two state are in agreement with the experimental values (**Table 1**) (**Figure 12**). Although the ground state and spin-two state have been calculated in other studies, these results are the first ab initio calculations of the Hoyle state with an energy close to the phenomenologically important ^{8}Be + α threshold. Note the energy-level crossing involving

Table 1 Lattice results for the ground state 0_1^+ and the low-lying excited states of ^{12}C (units: MeV)

	0_1^+	0_2^+	$2_1^+, J_z = 0$	$2_1^+, J_z = 2$
LO [$O(Q^0)$]	−110(2)	−94(2)	−92(2)	−89(2)
NLO [$O(Q^2)$]	−85(3)	−74(3)	−80(3)	−78(3)
N^{2}LO [$O(Q^3)$]	−91(3)	−85(3)	−88(3)	−90(4)
Experiment	−92.16	−84.51	−87.72	—

For comparison, the experimentally observed energies are shown. The error bars are 1-σ estimates that include both Monte Carlo statistical errors and uncertainties due to extrapolation at large Euclidean time. Systematic errors due to omitted higher-order interactions can be estimated from the size of corrections from $O(Q^0)$ to $O(Q^2)$ and from $O(Q^2)$ to $O(Q^3)$. Abbreviations: LO, leading order; NLO, next-to-leading order; N^{2}LO, next-to-next-to-leading order.

the Hoyle state and the spin-two state. The Hoyle state is lower in energy at LO but higher at NLO. One of the main characteristics of the NLO interactions is that the repulsion between nucleons is increased at short distances. This characteristic decreases the binding strength of the spinless states relative to higher-spin states. There is a 25-MeV reduction in the ground-state BE and a 20-MeV reduction for the Hoyle state but less than half as much binding correction for the spin-two state. This degree of freedom in the energy spectrum suggests that at least some fine-tuning of parameters is needed to set the Hoyle state energy near the ^{8}Be+^{4}He threshold. It would be very interesting to understand which fundamental parameters in nature control this fine-tuning. At the most fundamental level, there are only a few such parameters, of which two of the most interesting are the masses of the up and down quarks. Investigations have already been performed to unravel the quark mass dependence of the deuteron BE and of the *S*-wave *NN* scattering lengths (111, 112). The impact on the primordial abundances of light elements created by a variation of the quark masses at the time of big bang nucleosynthesis was studied in Reference 113.

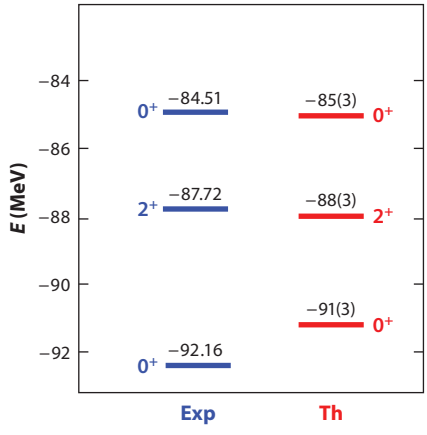

Figure 12

Results for the ^{12}C spectrum (Th) and comparison with experimental values (Exp). The results of the nuclear lattice effective field theory at next-to-next-to-leading order are shown for the ground state, the Hoyle state, and the lowest-lying spin-two state. In the simulations, the 2^+ state was split into the $J_z = 0$ and $J_z = 2$ projections. Only the $J_z = 0$ component is shown.

4.3. Neutron Matter

Not only is matter made exclusively of neutrons interesting in its own right; it is also of astrophysical relevance, given that various forms of this strongly interacting quantum many-body state are realized in the different layers of neutron stars. Due to the Pauli principle, three-body forces are suppressed in neutron matter, and of course, there is no Coulomb repulsion. As for nuclei, one can perform simulations for a fixed number of neutrons in a given volume, thereby varying the Fermi momentum k_F (density ρ) of the neutron matter. For N (spin-saturated) neutrons in a periodic cube of side length L, the Fermi momentum and density are

$$k_F = \frac{(3\pi^2 N)^{1/3}}{L}; \quad \rho = \frac{k_F^3}{3\pi^2}. \tag{31.}$$

Varying L from 4 to 7, and taking N to be 8, 12, or 16, corresponds to a Fermi momentum between 88 MeV and 155 MeV, that is, a density between 2% and 10% of normal nuclear matter density: $\rho_N = 0.17$ fm^3. Interestingly, neutron matter at $k_F \sim 80$ MeV is close to the so-called unitary limit, where the S-wave scattering length is infinite and the range of the interaction is negligible. At lower densities, corrections due to the (finite) scattering length become more important, and at higher densities, corrections due to the effective range and other effects become important. In the unitary limit, the ground state has no dimensionful parameters other than the particle density. Thus, the ground-state energy of the system should obey the simple relation $E_0 = \xi E_0^{\text{free}}$ for some dimensionless constant ξ, where E_0^{free} is the energy of noninteracting particles. The universal nature of the unitary limit makes it relevant to several areas of physics; in atomic physics, the unitarity limit has been studied extensively with ultracold ^{6}Li and ^{40}K atoms through the use of a magnetic-field Feshbach resonance (a summary of recent determinations of ξ can be found in Reference 114). There have been numerous analytic calculations of ξ that employ the full arsenal of available many-body techniques (see Reference 115 for a recent review). A benchmark calculation for the four-particle system was reported in Reference 114. Around the unitary limit, the ratio E_0/E_0^{free} can be parameterized as

$$\frac{E_0}{E_0^{\text{free}}} = \xi - \frac{\xi_1}{k_F a_{nn}} + \xi_2 k_F r_{nn} + \cdots \tag{32.}$$

in terms of the neutron-neutron (nn) scattering length a_{nn} and effective range r_{nn}. Below, we use $\xi = 0.31(1)$ and $\xi_1 = 0.81(1)$, as was determined from lattice simulations for two-component fermionic systems (116, 117).

Neutron matter has been studied in the framework of NLEFT (118, 119). **Figure 13** shows the energy of an N-neutron quantum state versus that of a free ensemble, in comparison to results from earlier calculations that used different many-body techniques. For most cases in the range of densities considered, the agreement is good. The universal parameter ξ_2 from Equation 32 ranges from 0.14 to 0.27 (119). In principle, this parameter can be measured in any two-component fermionic system.

In the future, nuclear lattice simulations of neutron matter could be used to investigate the interesting problem of a possible P-wave pairing, given that we can dial the strength of the nn interactions in the different partial waves by varying the strength of the corresponding LECs. Obviously, one cannot do so in nature. Also, simulations with greater numbers of neutrons and different lattice spacings will be necessary to better understand the neutron equations of state at higher densities and obtain better control over the lattice errors. Now that a neutron star of two solar masses has been observed (125), there are much more stringent constraints on the neutron equations of state (see, e.g., References 86 and 126), so future investigations based on NLEFT will be an important tool.

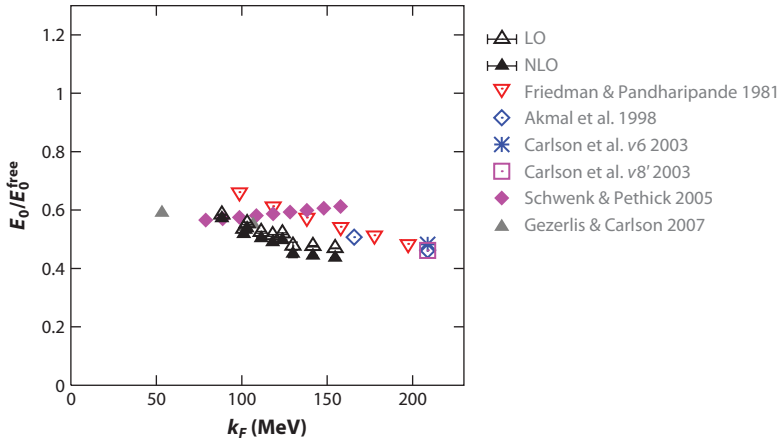

Figure 13

Results for the ground state of strongly interacting neutron matter E_0/E_0^{free} versus the Fermi momentum k_F in the framework of nuclear lattice effective field theory at leading order (LO) (*open triangles*) and next-to-leading order (NLO) (*filled triangles*). Also shown for comparison are the results from Friedman & Pandharipande (120), Akmal et al. (121), Carlson et al. *v*6 and *v*8′ (122), Schwenk & Pethick (123), and Gezerlis & Carlson (124), which are based on different many-body techniques.

DISCLOSURE STATEMENT

The authors are not aware of any affiliations, memberships, funding, or financial holdings that might be perceived as affecting the objectivity of this review.

ACKNOWLEDGMENTS

We thank all our collaborators for sharing their insights into the topics discussed here. We are also very grateful to Véronique Bernard, Hermann Krebs, and Dean Lee for useful comments on this manuscript. This work is partly supported by the Helmholtz Association through the Nuclear Astrophysics Virtual Institute (VH-VI-417); by the EU HadronPhysics3 project, "Study of strongly interacting matter"; by the European Research Council (ERC-2010-StG 259218 NucleArEFT); and by the Deutsche Forschungsgesellschaft (TR 16, "Subnuclear structure of matter").

LITERATURE CITED

1. Beane SR, Detmold W, Orginos K, Savage MJ. *Prog. Part. Nucl. Phys.* 66:1 (2011)
2. Weinberg S. *Phys. Lett. B* 251:288 (1990); Weinberg S. *Phys. Lett. B* 295:114 (1992); Weinberg S. *Nucl. Phys. B* 363:3 (1991)
3. Bernard V, Meißner U-G. *Annu. Rev. Nucl. Part. Sci.* 57:33 (2007)
4. Georgi H. *Annu. Rev. Nucl. Part. Sci.* 43:209 (1993)
5. Montvay I, Münster G. *Quantum Fields on a Lattice*. Cambridge, UK: Cambridge Univ. Press. 491 pp. (1994)
6. Epelbaum E, Hammer H-W, Meißner U-G. *Rev. Mod. Phys.* 81:1773 (2009)
7. Machleidt R, Entem DR. *Phys. Rep.* 503:1 (2011)
8. Platter L. *Proc. Sci.* 09:104 (2009)
9. Albaladejo M, Oller JA. *Phys. Rev. C* 84:054009 (2011)
10. Weinberg S. *Physica A* 96:327 (1979)
11. Coleman SR, Wess J, Zumino B. *Phys. Rev.* 177:2239 (1969)

12. Callan CG Jr, Coleman SR, Wess J, Zumino B. *Phys. Rev.* 177:2247 (1969)
13. Fettes N, Meißner U-G, Mojžiš M, Steininger S. *Ann. Phys.* 283:273 (2000); Fettes N, Meißner U-G, Mojžiš M, Steininger S. Erratum. *Ann. Phys.* 288:249 (2001)
14. Nambu Y. *Prog. Theor. Phys.* 5:82 (1950)
15. Taketani M, Mashida S, Onuma S. *Prog. Theor. Phys.* 7:45 (1952)
16. Okubo S. *Prog. Theor. Phys.* 12:603 (1954)
17. Epelbaum E, Glöckle W, Meißner U-G. *Nucl. Phys. A* 637:107 (1998); Epelbaum E, Glöckle W, Meißner U-G. *Nucl. Phys. A* 671:295 (2000); Epelbaum E, Glöckle W, Meißner U-G. *Nucl. Phys. A* 714:535 (2003)
18. Epelbaum E. *Phys. Lett. B* 639:456 (2006); Epelbaum E. *Eur. Phys. J. A* 34:197 (2007)
19. Kaiser N, Brockmann R, Weise W. *Nucl. Phys. A* 625:758 (1997)
20. Ordonez C, Ray L, van Kolck U. *Phys. Rev. C* 53:2086 (1996)
21. Kaiser N. *Phys. Rev. C* 61:014003 (2000); Kaiser N. *Phys. Rev. C* 62:024001 (2000); Kaiser N. *Phys. Rev. C* 64:057001 (2001)
22. Machleidt R. *Adv. Nucl. Phys.* 19:189 (1989)
23. Bernard V, Kaiser N, Meißner U-G. *Nucl. Phys. A* 615:483 (1997)
24. Epelbaum E, Krebs H, Meißner U-G. *Nucl. Phys. A* 806:65 (2008)
25. Fettes N, Meißner U-G, Steininger S. *Nucl. Phys. A* 640:199 (1998)
26. Buettiker P, Meißner U-G. *Nucl. Phys. A* 668:97 (2000)
27. Hemmert TR, Holstein BR, Kambor J. *J. Phys. G* 24:1831 (1998)
28. Fettes N, Meißner U-G. *Nucl. Phys. A* 679:629 (2001)
29. Kaiser N, Gerstendorfer S, Weise W. *Nucl. Phys. A* 637:395 (1998)
30. Krebs H, Epelbaum E, Meißner U-G. *Eur. Phys. J. A* 32:127 (2007)
31. Cohen TD, Hansen JM. *Phys. Rev. C* 59:13 (1999)
32. Cohen TD, Hansen JM. *Phys. Rev. C* 59:3047 (1999)
33. Epelbaum E, Gegelia J. *Eur. Phys. J. A* 41:341 (2009)
34. Epelbaum E. arXiv:1001.3229 [nucl-th] (2010)
35. Kaplan DB, Savage MJ, Wise MB. *Phys. Lett. B* 424:390 (1998); Kaplan DB, Savage MJ, Wise MB. *Nucl. Phys. B* 534:329 (1998)
36. Fleming S, Mehen T, Stewart IW. *Nucl. Phys. A* 677:313 (2000)
37. Epelbaum E, Glöckle W, Meißner U-G. *Nucl. Phys. A* 747:362 (2005)
38. Birse MC, McGovern JA. *Phys. Rev. C* 70:054002 (2004)
39. Birse MC. *Eur. Phys. J. A* 46:231 (2010)
40. Birse MC. *Phys. Rev. C* 76:034002 (2007)
41. Ipson KL, Helmke K, Birse MC. *Phys. Rev. C* 83:017001 (2011)
42. Rentmeester MCM, Timmermans RGE, Friar JL, de Swart JJ. *Phys. Rev. Lett.* 82:4992 (1999)
43. Entem DR, Machleidt R. *Phys. Rev. C* 68:041001 (2003)
44. Machleidt R. *Phys. Rev. C* 63:024001 (2001)
45. Gross F, Stadler A. *Phys. Rev. C* 78:014005 (2008)
46. Friar JL, van Kolck U. *Phys. Rev. C* 60:034006 (1999)
47. Friar JL, van Kolck U, Rentmeester MCM, Timmermans RGE. *Phys. Rev. C* 70:044001 (2004)
48. Epelbaum E, Meißner U-G. *Phys. Rev. C* 72:044001 (2005)
49. Epelbaum E. *Prog. Part. Nucl. Phys.* 57:654 (2006)
50. Nogga A, Timmermans RGE, van Kolck U. *Phys. Rev. C* 72:054006 (2005)
51. Pavon Valderrama M, Ruiz Arriola E. *Phys. Rev. C* 74:054001 (2006)
52. Epelbaum E, Meißner U-G. arXiv:nucl-th/0609037 (2006)
53. Beane SR, Kaplan DB, Vuorinen A. *Phys. Rev. C* 80:011001 (2009)
54. Lepage GP. arXiv:nucl-th/9706029 (1997)
55. Epelbaum E, Gegelia J. *Proc. Sci.* 09:077 (2009)
56. Birse MC. arXiv:1012.4914 [nucl-th] (2010)
57. Kalantar-Nayestanaki N, Epelbaum E, Messchendorp JG, Nogga A. *Rep. Prog. Phys.* 75:016301 (2012)
58. van Kolck U. *Phys. Rev. C* 49:2932 (1994)
59. Epelbaum E, et al. *Phys. Rev. C* 66:064001 (2002)
60. Ishikawa S, Robilotta MR. *Phys. Rev. C* 76:014006 (2007)

61. Bernard V, Epelbaum E, Krebs H, Meißner U-G. *Phys. Rev. C* 77:064004 (2008)
62. Bernard V, Epelbaum E, Krebs H, Meißner U-G. *Phys. Rev. C* 84:054001 (2011)
63. Friar JL, Coon SA. *Phys. Rev. C* 49:1272 (1994)
64. Skibinski R, et al. *Phys. Rev. C* 84:054005 (2011)
65. Machleidt R, Entem DR. *J. Phys. G* 37:064041 (2010)
66. Krebs H, Epelbaum E. *Few Body Syst.* 50:295 (2011)
67. Ishii N, Aoki S, Hatsuda T. *Phys. Rev. Lett.* 99:022001 (2007)
68. Doi T, et al. (HAL QCD Collab.) arXiv:1112.4103 [hep-lat] (2011)
69. Rozpedzik D, et al. *Acta Phys. Polon. B* 37:2889 (2006)
70. Glöckle W, et al. *Phys. Rep.* 274:107 (1996)
71. Deltuva A. *Eur. Phys. J. Web Conf.* 3:01003 (2010)
72. Kretschmer W, et al. *AIP Conf. Proc.* 339:335 (1995)
73. Witala H, et al. *Phys. Rev. C* 73:044004 (2006)
74. Duweke C, et al. *Phys. Rev. C* 71:054003 (2005)
75. Ley J, et al. *Phys. Rev. C* 73:064001 (2006)
76. Kistryn S, et al. *Phys. Rev. C* 72:044006 (2005)
77. Stephan E, et al. *Phys. Rev. C* 76:057001 (2007)
78. Stephan E, et al. *Phys. Rev. C* 82:014003 (2010)
79. Viviani M, et al. *Eur. Phys. J. Web Conf.* 3:05011 (2010)
80. Nogga A, Navratil P, Barrett BR, Vary JP. *Phys. Rev. C* 73:064002 (2006)
81. Navratil P, et al. *Phys. Rev. Lett.* 99:042501 (2007)
82. Gazit D, Quaglioni S, Navratil P. *Phys. Rev. Lett.* 103:102502 (2009)
83. Roth R, et al. *Phys. Rev. Lett.* 107:072501 (2011)
84. Navratil P, Quaglioni S, Stetcu I, Barrett BR. *J. Phys. G* 36:083101 (2009)
85. Otsuka T, et al. *Phys. Rev. Lett.* 105:032501 (2010)
86. Hebeler K, Lattimer JM, Pethick CJ, Schwenk A. *Phys. Rev. Lett.* 105:161102 (2010)
87. Holt JW, Kaiser N, Weise W. arXiv:1011.6623 [nucl-th] (2010)
88. Hagen G, Papenbrock T, Dean DJ. *Phys. Rev. C* 82:034330 (2010)
89. Lee D. *Prog. Part. Nucl. Phys.* 63:117 (2009)
90. Wigner E. *Phys. Rev.* 51:106 (1937)
91. Mehen T, Stewart IW, Wise MB. *Phys. Rev. Lett.* 83:931 (1999)
92. Chen J-W, Lee D, Schafer T. *Phys. Rev. Lett.* 93:242302 (2004)
93. Borasoy B, et al. *Eur. Phys. J. A* 31:105 (2007)
94. Meißner U-G. arXiv:1110.1721 [nucl-th] (2011)
95. Epelbaum E, Krebs H, Lee D, Meißner U-G. *Phys. Rev. Lett.* 106:192501 (2011)
96. Hubbard J. *Phys. Rev. Lett.* 3:77 (1959)
97. Stratonovich RL. *Sov. Phys. Dokl.* 2:416 (1958)
98. Weingarten DH, Petcher DN. *Phys. Lett. B* 99:333 (1981)
99. Scalettar RT, Scalapino DJ, Sugar RL. *Phys. Rev. B* 34:7911 (1986)
100. Gottlieb SA, Liu W, Toussaint D, Sugar RL. *Phys. Rev. D* 35:2611 (1987)
101. Duane S, Kennedy AD, Pendleton BJ, Roweth D. *Phys. Lett. B* 195:216 (1987)
102. Borasoy B, et al. *Eur. Phys. J. A* 35:343 (2008)
103. Epelbaum E, Krebs H, Lee D, Meißner U-G. *Eur. Phys. J. A* 41:125 (2009)
104. Borasoy B, et al. *Eur. Phys. J. A* 34:185 (2007)
105. Epelbaum E, Krebs H, Lee D, Meißner U-G. *Phys. Rev. Lett.* 104:142501 (2010)
106. Epelbaum E, Krebs H, Lee D, Meißner U-G. *Eur. Phys. J. A* 45:335 (2010)
107. Kreuzer S, Hammer H-W. *Phys. Lett. B* 694:424 (2011)
108. Hoyle F. *Astrophys. J. Suppl.* 1:121 (1954)
109. Kragh H. *Arch. Hist. Exact Sci.* 64:721 (2010)
110. Pieper SC. *Riv. Nuovo Cim.* 31:709 (2008)
111. Epelbaum E, Meißner U-G, Glöckle W. *Nucl. Phys. A* 714:535 (2003)
112. Beane SR, Savage MJ. *Nucl. Phys. A* 713:148 (2003)
113. Bedaque PF, Luu T, Platter L. *Phys. Rev. C* 83:045803 (2011)

114. Bour S, et al. *Phys. Rev. A* 83:063619 (2011)
115. Furnstahl RJ, Rupak G, Schäfer T. *Annu. Rev. Nucl. Part. Sci.* 58:1 (2008)
116. Lee D. *Phys. Rev. C* 78:024001 (2008)
117. Lee D. *Eur. Phys. J. A* 35:171 (2008)
118. Borasoy B, et al. *Eur. Phys. J. A* 35:357 (2008)
119. Epelbaum E, Krebs H, Lee D, Meißner U-G. *Eur. Phys. J. A* 40:199 (2009)
120. Friedman B, Pandharipande VR. *Nucl. Phys. A* 361:502 (1981)
121. Akmal A, Pandharipande VR, Ravenhall DG. *Phys. Rev. C* 58:1804 (1998)
122. Carlson J, Morales JJ, Pandharipande VR, Ravenhall DG. *Phys. Rev. C* 68:025802 (2003)
123. Schwenk A, Pethick CJ. *Phys. Rev. Lett.* 95:160401 (2005)
124. Gezerlis A, Carlson J. *Phys. Rev. C* 77:032801 (2008)
125. Demorest P, et al. *Nature* 467:1081 (2010)
126. Steiner AW, Lattimer JM, Brown EF. *Astrophys. J.* 722:33 (2010)

Annual Review of Nuclear and Particle Science

Volume 62, 2012

Contents

Indexes

Errata

An online log of corrections to *Annual Review of Nuclear and Particle Science* articles may be found at http://nucl.annualreviews.org/errata.shtml